Title	Biomechanical effects of hyper-dynamic cerebrospinal fluid flow through the cerebral aqueduct in idiopathic normal pressure hydrocephalus patients
Author(s)	Maeda, Shusaku; Otani, Tomohiro; Yamada, Shigeki et al.
Citation	Journal of Biomechanics. 2023, 156, p. 111671
Version Type	AM
URL	https://hdl.handle.net/11094/92339
rights	© 2023. This manuscript version is licensed under a Creative Commons Attribution-NonCommercial-NoDerivatives 4.0 International License.
Note	

1 **Biomechanical effects of hyper-dynamic cerebrospinal fluid flow through the**

2 **cerebral aqueduct in idiopathic normal pressure hydrocephalus patients**

3 Shusaku Maeda[1], Tomohiro Otani[1], Shigeki Yamada[2,3,4], Yoshiyuki Watanabe[3], Selin Yavuz Ilik[1],

4 Shigeo Wada[1]

5 *[1] Graduate School of Engineering Science, Osaka University, 1-3 Machikaneyamacho,*
6 *Toyonaka, Osaka, 560-8531, Japan*

7 *2 Department of Neurosurgery, Nagoya City University Graduate School of Medical Science, 1*
8 *Kawasumi, Mizuho-cho, Mizuho-ku, Nagoya, Aichi, 467-8601, Japan*

9 *3 Interfaculty Initiative in Information Studies / Institute of Industrial Science, The University of*
10 *Tokyo, Tokyo, Japan*

11 *[4] Department of Neurosurgery, Shiga University of Medical Science, Setatsukinowacho, Otsu,*
12 *Shiga, 520-2192, Japan*
13 *5 Department of Radiology, Shiga University of Medical Science, Setatsukinowacho, Otsu,*
14 *Shiga, 520-2192, Japan*
15

16 Type: Original Article

17

18 Address for Correspondence:

19 Tomohiro Otani, PhD

20 Department of Mechanical Science and Bioengineering,

21 Graduate School of Engineering Science, Osaka University

22 1-3 Machikaneyamacho, Toyonaka, Osaka, 560-8531, Japan

23 Phone: +81-6-6850-6174

24 E-mail: otani.tomohiro.es@osaka-u.ac.jp

25

28

29 Word count: 3500

Abstract

Normal pressure hydrocephalus (NPH) is an intracranial disease characterized by an abnormal accumulation of cerebrospinal fluid (CSF) in brain ventricles within the normal range of intracranial pressure. Most NPH in aged patients is idiopathic (iNPH) and without any prior history of intracranial diseases. Although an abnormal increase of the CSF stroke volume (hyper-dynamic CSF flow) in the aqueduct between the third and fourth ventricles in iNPH patients has received much attention as a clinical evaluation index, biomechanical effects of this flow on iNPH pathophysiology are poorly understood. This study aimed to clarify the potential biomechanical effects of hyper-dynamic CSF flow through the aqueduct of iNPH patients using magnetic resonance imaging-based computational simulations. Ventricular geometries and CSF flow rates through aqueducts of 10 iNPH patients and 10 healthy control subjects were obtained from multimodal magnetic resonance images, and these CSF flow fields were simulated using computational fluid dynamics. As biomechanical factors, we evaluated the wall shear stress on the ventricular wall and the extent of flow mixing, which potentially disturbs the CSF composition in each ventricle. The results showed that the relatively high CSF flow rate and large and irregular shapes of the aqueduct in iNPH resulted in large wall shear stresses localized in relatively narrow regions. Furthermore, the resulting CSF flow showed stable cyclic motion in control subjects, whereas strong mixing during transport was found through the aqueduct in patients with iNPH. These findings provide further insights into the clinical and biomechanical correlates of NPH pathophysiology.

1   Introduction

53   Cerebrospinal fluid (CSF) fills brain ventricles and subarachnoid spaces and enables

54   homeostatic transport of nutrients and hormones (May et al., 1990). Abnormal accumulation of

55   CSF in the ventricles within normal ranges of intracranial pressure is called normal pressure

56   hydrocephalus (NPH; Marmarou et al., 2005) and causes multiple dysfunctions, such as cognitive

57   impairment, gait disturbance, and urinary incontinence (Mori et al., 2012). In particular,

58   idiopathic NPH (iNPH) is a major form of NPH observed in aged patients without prior history of

59   intracranial disease. Because of its association with aging and cognitive dysfunction (Nakajima et

60   al., 2021), the etiology and pathophysiology of iNPH have received much attention from medical

61   (Zhangyang et al., 2020) and biomechanical (Linninger et al., 2016) researchers.

62   Hyper-dynamic CSF flow in the aqueduct (the flow pathway through the third and fourth

63   ventricles) has been widely reported in phase-contrast magnetic resonance imaging (PCMRI)

64   studies of iNPH patients as a part of disease progression (Bradley et al., 1996; Scollato et al., 2008;

65   Shanks et al., 2019). CSF flow in the aqueduct is pulsatile and bidirectional, synchronizing with

66   cerebral arterial expansion during the cardiac cycle (Bradley et al., 1996; Brinker et al., 2014;

67   Enzmann et al., 1993). However, characterization of hyper-dynamic CSF flow through the

68   aqueduct has been limited to a clinical diagnostic index, and the associations of biomechanical

69   effects with intracranial homeostasis and pathophysiology are poorly understood.

70   This study considered two biomechanical effects of the hyper-dynamic CSF flow through the

71   aqueduct in iNPH patients. The first is an abnormal mechanical stimulus against the ependymal

72   cells lining the aqueduct lumens. Since malfunction of the motile cilia of the ependymal cells

73   occurs during hydrocephalus (Lechtreck et al., 2008; Shook et al., 2014), greater CSF flow may

74   result in a physiologically inappropriate mechanical stimulus on the ependymal cells and affect

75   their functions (Yamada et al., 2021). The second biomechanical effect is an abnormal mixing of

76   CSF between third and fourth ventricles through the aqueduct. The CSF contains proteins and

77   signaling molecules in the form of actively released neuroactive substances (Nicholson, 1999;

78   Skipor and Thiery, 2008), which are mainly produced by the epithelium of the choroid plexus

79   located in each ventricle (Damkier et al., 2013): the CSF composition varies among the ventricles

80   in normal conditions (Cavanagh et al., 1983; Lun et al., 2015; Zappaterra et al., 2007). Abnormal

81   mixing of CSF compositions has been observed in the ventricular and subarachnoid spaces

82   (Ringstad et al., 2017) and lumbar and ventricular regions (Puy et al., 2016) in iNPH patients.

83   These abnormalities in CSF flow and the chemical environment of the CSF have been associated

84   with depression, cognitive dysfunction, and nervous system disorders (Attier-Zmudka et al.,

85   2019; Bothwell et al., 2019; Seo et al., 2021). These findings suggest that mixing of CSF through

86   aqueducts disturbs the individual CSF compositions of the third and fourth ventricles and is

87   associated with pathologic conditions. We therefore hypothesized that hyper-dynamic CSF flow

88   through the aqueduct has potential biomechanical effects on intracranial homeostasis.

89   Understanding these effects may link characteristic CSF flow profiles observed in clinical practice

90   with existing biomechanical knowledge regarding iNPH pathophysiology.

91   　　This study aimed to clarify the biomechanical effects of hyper-dynamic CSF flow through the

92   cerebral aqueduct between the third and fourth ventricles of iNPH patients by combining MRI

93   measurements and computational simulations. Subject-specific ventricle geometries and

94   aqueduct flow rates were acquired from T2-weighted MRI and four-dimensional (4D) flow MRI

95 measurements, respectively, of 10 iNPH patients and 10 healthy controls. Based on these data,

96 computational fluid dynamics simulations of CSF flow in the ventricles of each patient were

97 conducted. The mechanical effects of normal CSF flow and CSF flow mixing on the ventricle were

98 analyzed using the CSF flow velocity field obtained from computational simulations.

99 **2   Materials and Methods**

100 **2.1   Study participants**

101   Participants included 10 iNPH patients (six male, four female; age range, 61–83 y; iNPH1–

102 iNPH10) diagnosed following the Japanese clinical guidelines for iNPH (Nakajima et al., 2021) and

103 10 healthy controls (seven male, three female; age range, 22–47 y; control1–control10) who

104 received treatment at the Department of Neurosurgery, Shiga University of Medical Science

105 Hospital in 2018–2021. Inclusion criteria for iNPH patients and healthy controls are described in

106 Supplementary 1. The study was approved by the Institutional Review Boards of Shiga University

107 of Medical Science (No. R2019-227) and Osaka University (No. R2-1). Patients were included after

108 they gave oral and written informed consent.

109   Image acquisition was performed for each subject using a 3-T MRI scanner (Discovery MR

110 750W, GE Healthcare, Milwaukee, WI, USA). Three-dimensional velocity-encoded data were

111 obtained using the 4D flow MRI sequence with 5 cm/s velocity encoding (0.7813 mm × 0.7813

112 mm × 1.0 mm) and eight phases of the cardiac cycle were reconstructed. Furthermore, to

113 construct patient-specific geometries of the brain ventricles, we used volumetric data obtained

114 from a T2-weighted sequence (0.8 mm × 0.8 mm × 0.8 mm). Measurement details are shown in

115 Supplementary 2.

2.2 Image processing

Ventricle geometries were extracted from T2-weighted MRI data and reconstructed as a set of triangular surfaces using Mimics (Version 23; Materialize Inc., Yokohama, Japan). Table 1 shows basal geometric properties of the aqueduct and ventricles in all patients, in which the measurement protocol is shown in Supplementary 3. Representative geometries of controls and iNPH patients are shown in Fig. 1(A) and (B), and variations in the aqueduct cross-sectional area are summarized in Fig. 1(C). In controls, the aqueduct cross-sectional area monotonically decreased from the fourth to the third ventricle and ranged from 1.67 to 39.0 mm^2. In contrast, the corresponding area in iNPH patients had a local minimum near the center of the aqueduct and relatively large variation ranging from 2.34 to 46.8 mm^2. The absolute minimum aqueduct diameter was 1.46 mm and 2.32 mm in controls and iNPH patients, respectively.

Next, the time course of the CSF flow rate through the aqueduct was obtained using 4D flow MRI. Aliasing artifacts and eddy-current-based phase offsets were eliminated following the methods used in our previous study (Yavuz Ilik et al., 2022). To consider the characteristic features of CSF flow in the aqueduct, we computed the Reynolds number ($\mathrm{Re} = \rho U D / \mu$) and Womersley number ($\mathrm{Wo} = D \left(\omega \rho / \mu \right)^{\frac{1}{2}}$) as non-dimensional indices, where ρ is the density, μ is the viscosity, U is average velocity through the aqueduct cross-section, ω is the circular frequency of oscillatory flow in the aqueduct calculated from the cardiac cycle, and D is the equivalent diameter of the aqueduct cross-section. Following experimental data, we defined ρ = 1×10^3 kg/m^3 and μ = 1×10^{-3} Pa·s (Bloomfield et al., 1998). Validities of the 4D flow MRI data was confirmed in Appendix 1.

2.3 Numerical simulation

CSF domains were spatially discretized using first-order tetrahedral elements with a base mesh size of 0.7 mm and three layers of boundary prism layer elements using ICEM CFD (Version 2021 R2; ANSYS Inc., Canonsburg, USA). The mesh size independency test was conducted as noted in Supplementary 4. The CSF was modeled as an incompressible Newtonian fluid based on existing experimental data (Bloomfield et al., 1998). We modeled the CSF flow as being driven by arterial pulsations without CSF production because the influence of CSF production is relatively small over this time scale (Bradley, 2015). On the basis of this assumption, we expressed CSF flow as a transient volume change in the lateral ventricles (LVs) equivalent to the aqueduct flow rate. Thus, CSF flow was expressed by the equation of continuity and incompressible Navier–Stokes equation in arbitrary Lagrangian–Eulerian form for moving-wall boundary problems, given by

$$\nabla \cdot \mathbf{v} = 0, \tag{1}$$

$$\rho\left(\partial_t \mathbf{v} + \tilde{\mathbf{v}} \cdot \nabla \mathbf{v}\right) = -\nabla p + \mu \nabla^2 \mathbf{v}, \tag{2}$$

where $\mathbf{v}$ is the velocity vector, $\tilde{\mathbf{v}}$ is the advection velocity in the arbitrary Lagrangian–Eulerian coordinates, and p is the pressure. These equations were spatially discretized in a finite element manner using a streamline upwind Petrov–Galerkin formulation (Bazilevs et al., 2012) and computed by fractional step method. Computational details are briefly introduced in Supplementary material 5.

Regarding computational conditions, we set prescribed moving-wall boundary conditions on the LV surface. The LV motion was simplified by assuming isotropic volume expansion and contraction, and the rate of the LV volume change was set to the aqueduct flow rate measured

158   using 4D flow MRI (Fig. 2(A)), following Sweetman et al. (2011). Uniform displacement was

159   assigned on each LV surface node and its direction was set to unit surface normal. Cut-sections of

160   the foramen of Magendie and foramen of Luschka were set to a fixed pressure boundary

161   condition of 0 Pa. The time increment was set to 1×10^{-3} s to satisfy a Courant–Friedrichs–Lewy

162   number < 0.15. Computational simulations were conducted through four cardiac cycles for each

163   subject. In section 3, we show results from the fourth cardiac cycle unless otherwise noted.

164   **2.4   Evaluation indices**

165   First, we evaluated spatial distributions of wall shear stress (WSS) on the aqueduct surface

166   at the time of maximum CSF flow rate from the third to fourth ventricles to consider mechanical

167   stimulus associated with the hyper-dynamic CSF flow. Following previously described methods,

168   WSS was computed in each element using the shear stress tensor $\frac{1}{2}\mu\left(\nabla\mathbf{v}^{\top}+\nabla\mathbf{v}\right)$ and surface

169   unit normal (Sotelo et al., 2015). Next, we evaluated CSF flow mixing through the aqueduct using

170   massless particle tracers. The tracers were positioned at intervals of 0.25 mm along the aqueduct

171   with respect to each direction in Cartesian coordinates, and their motions were tracked through

172   20 cardiac cycles. Particle motions were expressed using the flow velocity vector $\mathbf{v}$, given by

$$\frac{d\mathbf{x}_i}{dt} = \mathbf{v}, \tag{3}$$

174   where $\mathbf{x}_i$ is the position vector of the particle i. Eq. (3) was iteratively solved using the fourth-

175   order Runge–Kutta method. For quantitative evaluation of the mixing using these particle tracers,

176   we computed the mix-norm (Mathew et al., 2005) adjusted for discrete particle mixing as

177   described by Arzani et al. (2014). The mix-norm is a multi-scale mixing index that assesses the

178 mixing extent and ranges from zero (not mixed) to one (completely mixed). A brief definition and

179 computation of the mix-norm are shown in Appendix 2 for completeness. To compute the mix-

180 norm, the approximate shape of the aqueduct was defined from the reconstructed surface as a

181 domain between the third and fourth ventricles with a diameter less than twice the minimum

182 diameter. Differences in the anatomical and physical data between iNPH patients and control

183 subjects were assessed statistically using the Mann–Whitney U test (SciPy v1.6.2 software;

184 https://scipy.org/).

185 **3   Results**

186   Figure 2(A) shows the time courses of CSF flow rate (A) in the aqueduct on 4D flow MRI. Flow

187 from the fourth to the third ventricle was deemed positive and the cardiac cycle was considered

188 to start at early systole. The flow rate showed a pulsatile motion with a negative value in systole

189 and a positive value in diastole. The maximum flow rate in iNPH patients was approximately

190 three-fold higher than that in controls (p < 5 × 10^{-3}). Figure 2(B) and (C) showed the maximum Re

191 and Wo. Significant differences of these both numbers were found between iNPH patients (Re:

192 58.0 ± 27.6, Wo: 0.86 ± 0.14) and controls (Re: 13.7±8.3, Wo: 1.50 ± 0.32) (Re: $p < 1 \times 10^{-3}$ and

193 Wo: $p < 5 \times 10^{-4}$).

194   Figure 3 shows WSS spatial distributions on the aqueduct surface in representative control

195 and iNPH cases (iNPH2, control1). WSS magnitudes were almost constant in controls (Fig. 3(A)),

196 whereas high WSS values were found in relatively narrow domains in iNPH (Fig. 3(B)). For

197 quantitative comparisons of these tendencies, we computed WSS distributions along the

198 longitudinal direction of the aqueduct. The average WSS magnitude ranged from 8 to 25 mPa in

199   controls, whereas that in iNPH patients was approximately three-fold higher and ranged from 23

200   to 78 mPa (p = 1.7×10^{-3}). Furthermore, spatial variations of the WSS magnitude in iNPH patients

201   were 5–6-fold larger than those in controls, and stresses were localized in the center region with

202   relatively narrow cross-sections. CSF stroke volumes and peak WSS magnitudes are summarized

203   in Supplementary 6.

204   The CSF mixing states in the aqueduct were analyzed using massless particle tracing through

205   20 cardiac cycles. Figure 4 shows representative snapshots of the particle tracer distributions

206   from the initial state to fourth cardiac cycle in the aqueduct in control1 and iNPH2. In controls,

207   the particle tracer showed a slight but steady cyclic motion (Supplementary 7). In contrast, in

208   iNPH patients, relatively strong mixing with particle transfers between ventricles through the

209   aqueduct was found (Supplementary 8).

210   Figure 5 illustrates the particle tracer distributions in all subjects after 20 cardiac cycles. The

211   particle distribution remained almost the same as that in the initial setting in all controls, while

212   the distribution in iNPH patients showed notable variety and mixing, especially in iNPH2 and

213   iNPH8. In these cases, particle tracers were cyclically moved following CSF convection

214   synchronized with the cardiac cycle and gradually drifted from their initial positions. Particles

215   located in the third ventricles reached the fourth ventricle through the aqueduct within 20

216   cardiac cycles, and vice versa. We computed the mix-norm in each subject for the quantitative

217   evaluation of the CSF mixing state from particle tracers in the aqueduct. Figure 6 shows the time

218   courses of the mix-norm in the aqueduct in all participants. In the controls, the mix-norm

219   moderately increased and remained under 0.5 in all cases even after 20 cardiac cycles. In contrast,

220   iNPH patients tended to have a steep increase and wide patient-specific variation of the mix-

221   norm from 0.2 to 0.9 after 20 cardiac cycles. The median values of the mix-norm after 20 cardiac

222   cycles were 0.314 and 0.523 in controls and iNPH patients, respectively, and these values were

223   significantly different ($p = 7 \times 10^{-3}$).

224   **4   Discussion**

225   The hyper-dynamic CSF flow through the aqueduct between third and fourth ventricle is

226   widely known as a part of iNPH progression (Scollato et al., 2008), while these the biomechanical

227   effect of the hyper-dynamic CSF flow remains unclear. To address this issue, this study

228   investigated CSF flow dynamics through the aqueduct in iNPH patients and control subjects using

229   MRI-based computational simulations. MRI showed that iNPH patients have characteristic

230   properties, including large ventricles, as summarized in the clinical guideline (Nakajima et al.,

231   2021), and a relatively high CSF flow rate (Fig. 2), consistent with existing clinical reports (Bradley,

232   2015). Based on these MRI measurements, the CSF flow dynamics in each patient were

233   determined using computational simulations, and biomechanical properties, such as wall shear

234   stress and flow mixing, were evaluated.

235   To consider the size of the mechanical stimulus associated with the CSF flow enhancements,

236   we evaluated the peak WSS on the aqueduct surface. Although WSS analyses on the aqueduct

237   surface have been performed using images from 4D flow MRI (e.g., Yamada et al., 2020, 2021),

238   there are strong severe concerns about their accuracy because of limitations in spatial resolution

239   and use of eddy-current-based offsets to measure small flow velocities (Wentland et al., 2010),

240   which needs appropriate offset eliminations (e.g., Yavuz Ilik et al., 2022) to address the above

241   concerns and obtain reasonable WSS profiles. The obtained results showed that iNPH causes not

242 only approximately 3-fold larger base WSS values compared with control subjects but also 5–6-

243 fold larger WSS variations (Fig. 3) associated with the geometric alteration shown in Fig. 1. These

244 differences indicate that ependymal cells on the aqueduct surface are exposed to abnormal local

245 mechanical stimuli in iNPH. Because the relatively large WSS causes damage to the ependymal

246 cells with loss of the motile cilia and this damage associates with pathologic events (Shook et al.,

247 2014), the characteristic mechanical stimulus in iNPH patients may induce further pathologic

248 states in ventricular environments.

249 Hyper-dynamic CSF flow in iNPH patients, observed using PCMRI, significantly impacted flow

250 dynamics associated with CSF flow mixing. In controls, the effects of CSF convection were

251 moderate (Re ≈ 30), and the CSF flow profile had spatially uniform properties in the longitudinal

252 direction. These moderate flow characteristics resulted in stable cyclic flow during pulsatile

253 motion (Fig. 5). In contrast, the CSF flow in iNPH patients showed convection-dominant (Re ≈

254 100) and non-negligible unsteady (Wo ≈ 2) profiles. Enhancement of the CSF mixing in the

255 aqueduct associated with iNPH progression, as demonstrated in this study, has clinical and

256 pathophysiological implications. Associations between CSF flow and neurological diseases have

257 recently attracted attention from a biochemical perspective (Attier-Zmudka et al., 2019;

258 Bothwell et al., 2019; Puy et al., 2016; Seo et al., 2021) and suggested associations between

259 characteristic CSF flow alterations in iNPH patients and mixing of the CSF composition (Puy et al.,

260 2016). Clinical studies reported that hyper-dynamic CSF flow through the aqueduct was

261 associated with iNPH progression (Scollato et al., 2008) and this stabilization related to surgical

262 outcomes (Shanks et al., 2019). Furthermore, MRI measurements of CSF flow dynamics using

263 contrast agents revealed CSF mixing between the ventricle and subarachnoid space in iNPH

264 patients (Ringstad et al., 2017) and CSF flow stasis in the ventricle after shunt surgery (Kawaguchi

265 et al., 2011). The obtained results are consistent with these clinical observations and thus indicate

266 the significance of CSF flow dynamics in iNPH patients in CSF flow mixing from a fluid mechanics

267 perspective. Therefore, we suggest that enhancement of the CSF mixing in the aqueduct in iNPH

268 patients is not only a diagnostic criterion but also a possible factor that induces neurological

269 symptoms associated with iNPH progression.

270   This study has three main limitations. First, the number of participants and their sex and age

271 distributions were limited. However, because geometric and CSF flow differences between iNPH

272 patients and controls were consistent with prior measurements (Bradley et al., 1996; Bradley,

273 2015), we believe the limited data did not critically affect the qualitative findings of our study.

274 Nevertheless, further consideration using large population data should be conducted to provide

275 a more comprehensive understanding of CSF flow characteristics. Second, this study considered

276 CSF flow dynamics synchronized with cardiac pulsation measured using 4D flow MRI without

277 considering other factors, such as respiratory motion, motile cilia, net CSF flow, and aqueduct

278 wall motions. CSF flow measurements using other modalities have highlighted the influence of

279 respiratory motion(Yamada et al., 2013), although the extent of its effect on CSF flow in the

280 aqueduct remains controversial (Sincomb et al., 2020). Moreover, in vivo measurements of CSF

281 dynamics using model animals showed motile cilia of ependymal cells present on the ventricle

282 surfaces drive CSF flow (Faubel et al., 2016; Shook et al., 2014) to compartmentalize the CSF

283 within individual ventricles (Olstad et al., 2019). Nevertheless, it remains unknown whether these

284 findings from experimental studies in small animals can accurately model CSF pathophysiology in

285 human ventricles (Ringers et al., 2020). In particular, global CSF flow in the ventricles can be

286　considered to be dominantly driven by the pulsatile motion related to the heartbeat, and the role

287　of the motile cilia seems to be localized in the near-wall flow field (Siyahhan et al., 2014). Further

288　investigations regarding the possible effects of motile cilia on CSF flow and mixing could address

289　the above question. In addition, net CSF flow through the aqueduct was not treated in this study

290　because it considered CSF flow over a relatively short period of at most 20 cardiac cycles.

291　Nevertheless, the net flow may affect the long-term CSF mixing states observed in biochemical

292　studies. Lastly, since the aqueduct wall motion cannot be detected in MRI with the voxel size of

293　the sub-mm scales, we assumed the aqueduct wall as rigid in computation. Although we believe

294　these effects are secondary on qualitative tendencies, wall motion may affect quantitative values,

295　especially the WSS, and subscale flow characteristics as well as primally cilia. Third, because of

296　limitations in spatiotemporal resolution, background noise, and artifacts in the 4D flow MRI, we

297　used the total CSF flow rate as a computational condition and did not assess the spatiotemporal

298　flow velocity map directly. Although 2D PCMRI with multiple slices can increase the

299　spatiotemporal resolution, we used 4D flow MRI because it can effectively detect complex CSF

300　movements in all three spatial directions in a limited scan time. Temporal resolution was limited

301　by the actual MRI scan time, which was chosen to minimize patient burden. The measurement

302　CSF flow profiles showed significant differences between controls and iNPH patients, consistent

303　with current understanding (Bradley, 2015), and thus we believe that the limited temporal

304　resolution did not affect the conclusions of this study. To address this issue, data assimilations

305　using MRI data (e.g, Otani et al., 2022) may be capable to obtain CSF flow characteristics in the

306　entire ventricles rather than just through the aqueducts.

307   In conclusion, this study investigated the biomechanical effects of the hyper-dynamic CSF flow

308   through the aqueduct in iNPH patients using MRI-based computational simulations. CSF flow

309   fields in the ventricles in 10 healthy controls and 10 iNPH patients were computed and

310   mechanical stimuli and flow mixing states were evaluated. The obtained results demonstrated

311   that iNPH causes high WSS values in relatively narrow regions of the aqueduct and significantly

312   enhances the CSF flow mixing between ventricles. These findings suggest that hyper-dynamic CSF

313   flow in iNPH results in significantly different fluid dynamical properties in the aqueduct in iNPH

314   patients compared with healthy individuals and thus provide further insight into clinical and

315   biological correlates of iNPH pathophysiology.

316

317   **Appendix 1. Spatiotemporal validities of the 4D flow MRI**

318   Validities of spatiotemporal resolution of 4D flow MRI data were confirmed from

319   following two investigations. First, we evaluated spatial continuity of CSF flow rate through the

320   aqueduct, as a validation of the spatial resolution. Time courses of the CSF flow rate during a

321   cardiac cycle were extracted on representative four cross-sectional planes of the aqueduct and

322   these average and standard deviation were evaluated in a control subject (control8) and an iNPH

323   patient (iNPH8), as representatives (Fig. A1(A)). Standard variations were at most 5% of the

324   average in both two cases, and thus we confirmed that the MRI data using in this study has

325   acceptable spatial continuities of the CSF flow rate through the aqueduct. Next, we evaluated

326   the net CSF flow and the CSF stroke volume through the aqueduct, as a validation of temporal

327   resolution. Fig. A1 (B) shows the box plots of the net CSF flow and stroke volume through the

328   aqueduct in one cardiac cycle in all healthy controls and iNPH patients. The net CSF flow volume

329   in controls and iNPH patients were 0.43±0.46 µl and 1.95±1.48 µl, respectively, and were at most

330   10% or less of this CSF stroke volume. Because the net CSF flow are negligibly small comparing to

331   the stroke volume (Bradley et al., 1996), these results are consistent with existing physiological

332   knowledge. From these validation studies, we concluded that the MRI data using in this study has

333   appropriate qualities to obtain the CSF flow rate through aqueducts.

334

335   **Appendix 2. Definition and computation of the mix-norm**

336   The mix-norm is an established multiscale measure of mixing (Mathew et al., 2005). In the

337   original definition, the mix-norm in the case of a one-dimensional torus

338    $S^1 = [0,1]$ is obtained by integrating the square of the average values of the function

339    $c : S^1 \rightarrow \mathbb{R}$ over a dense set of subsets contained in S^1. First, the mean value of c within the

340   interval $s \in (0,1)$ around $p \in [0,1]$ is given by

341
$$d(c,p,s) = \frac{1}{s} \int_{p-\frac{1}{2}}^{p+\frac{1}{2}} c(x)\mu(dx), \tag{4}$$

342   where μ is the Lebesgue measure. The mix-norm $\phi(c)$ is defined as the L^2 norm of the

343   function $d(c,p,s)$ averaged with respect to p and s, such that

344
$$\varphi(c,s) = \left(\int_{S^1} d^2(c,p,s)\mu(dp) \right)^{\frac{1}{2}}, \tag{5}$$

345   and then

16

$$\phi(c) = \left(\int_{S^1} \varphi^2(c,s)\mu(ds) \right)^{\frac{1}{2}}. \tag{6}$$

This definition was generalized to a multi-dimensional torus following a straightforward process (Mathew et al., 2005).

Arzani et al. (2014) used the mix-norm to evaluate the extent of discrete particle mixing in the domain of interest Γ from time t to $t + \Delta t$. First, they divided the domain Γ into equally-spaced subdomains $\Gamma_i(s_j)$ given by

$$\Gamma = \bigcup_{i=1}^{N_{s_j}} \Gamma_i(s_j), \tag{7}$$

where N_{s_j} is the total number of subdomains and s_j is the particular length scale used to form them. The function $c_i(s_j, \Delta t)$ was defined as the percentage of remaining particles in the region of interest in a finite time, such that

$$c_i(s_j, t + \Delta t) = \frac{N_{out}}{N_{in} + N_{out}}, \tag{8}$$

where N_{in} and N_{out} are the number of particles in $\Gamma_i(s_j)$ at time $t + \Delta t$ while inside and outside, respectively, at time t. Following the definitions in Eqs. (1)–(3), the mix-norm can be computed as the root mean square of c_i, as in the original definition. In the present study, we considered four different length scales to define s_j, which divided the aqueduct into 2, 4, 8, or 10 subdomains.

363 **Supplementary material**

364 Supplementary material 1: Inclusion criteria for iNPH patients and healthy controls

365 Supplementary material 2: Image acquisition details

366 Supplementary material 3: Geometric properties of the aqueduct and ventricles

367 Supplementary material 4: Mesh size independency test

368 Supplementary material 5: Computational details

369 Supplementary material 6: CSF stroke volume and peak wall shear stress in the aqueduct

370 Supplementary material 7: Video of particle tracking in the cerebral aqueduct of a healthy control

371 Supplementary material 8: Video of particle tracking in the cerebral aqueduct of an iNPH patient

372

381

382 **Conflict of interest statement**

383 The authors declare that the research was conducted in the absence of any commercial or

384 financial relationships that could be construed as a potential conflict of interest.

385

386 **5 References**

387 Ambarki, K., Israelsson, H., Wåhlin, A., Birgander, R., Eklund, A., Malm, J.,
388 2010. Brain ventricular size in healthy elderly: Comparison between
389 evans index and volume measurement. Neurosurgery 67, 94–99.
390 https://doi.org/10.1227/01.NEU.0000370939.30003.D1

391 Arzani, A., Les, A.S., Dalman, R.L., Shadden, S.C., 2014. Effect of exercise on
392 patient specific abdominal aortic aneurysm flow topology and mixing.
393 Int J Numer Method Biomed Eng 30, 280–295.
394 https://doi.org/10.1002/cnm

395 Attier-Zmudka, J., Sérot, J.M., Valluy, J., Saffarini, M., Macaret, A.S., Diouf,
396 M., Dao, S., Douadi, Y., Piotr Malinowski, K., Balédent, O., 2019.
397 Decreased cerebrospinal fluid flow is associated with cognitive deficit
398 in elderly patients. Front Aging Neurosci 11, 1–8.
399 https://doi.org/10.3389/fnagi.2019.00087

400 Bazilevs, Y., Takizawa, K., Tezduyar, T.E., 2012. Computational fluid-
401 structure interaction. John Wiley & Sons, Ltd.
402 https://doi.org/10.1002/9781118483565

403 Bloomfield, I.G., Johnston, I.H., Bilston, L.E., 1998. Effects of proteins, blood
404 cells and glucose on the viscosity of cerebrospinal fluid. Pediatr
405 Neurosurg 28, 246–251. https://doi.org/10.1159/000028659

406 Bothwell, S.W., Janigro, D., Patabendige, A., 2019. Cerebrospinal fluid
407 dynamics and intracranial pressure elevation in neurological diseases.
408 Fluids Barriers CNS 16, 1–18. https://doi.org/10.1186/s12987-019-
409 0129-6

410 Bradley, W.C., Scalzo, D., Queralt, J., Nitz, W.N., Atkinson, D.J., Wong, P.,
411 1996. Normal-Pressure Hydrocephalus: Evaluation with Cerebrospinal
412 Fluid Flow Measurements at MR Imaging. Radiology 198, 523–529.

413   Bradley, W.G., 2015. CSF Flow in the Brain in the Context of Normal
414   Pressure Hydrocephalus. AJNR Am J Neuroradiol 36, 831–838.
415   https://doi.org/10.3174/ajnr.A4124

416   Brinker, T., Stopa, E., Morrison, J., Klinge, P., 2014. A new look at
417   cerebrospinal fluid circulation. Fluids Barriers CNS 11, 10.
418   https://doi.org/10.1186/2045-8118-11-10

419   Cavanagh, M.E., Cornelis, M.E.P., Dziegielewska, K.M., Evans, C.A.N.,
420   Lorscheider, F.L., Møllgård, K., Reynolds, M.L., Saunders, N.R., 1983.
421   Comparison of proteins in CSF of lateral and IVth ventricles during early
422   development of fetal sheep. Developmental Brain Research 11, 159–
423   167. https://doi.org/10.1016/0165-3806(83)90213-4

424   Damkier, H.H., Brown, P.D., Praetorius, J., 2013. Cerebrospinal fluid
425   secretion by the choroid plexus. Physiol Rev 93, 1847–1892.
426   https://doi.org/10.1152/physrev.00004.2013

427   Enzmann, D.R., Pelc, N.J., McComb, J.G., 1993. Cerebrospinal fluid flow
428   measured by phase-contrast cine MR. American Journal of
429   Neuroradiology 14, 1301-1307+1309.

430   Faubel, R., Westendorf, C., Bodenschatz, E., Eichele, G., 2016. Cilia-based
431   flow network in the brain ventricles. Science (1979) 353, 176–178.
432   https://doi.org/10.1126/science.aae0450

433   Kawaguchi, T., Hirata, Y., Bundo, M., Kondo, T., Owaki, H., Ito, S.,
434   Hashimoto, M., Ishikawa, M., 2011. Role of computerized tomographic
435   cisternography in idiopathic normal pressure hydrocephalus. Acta
436   Neurochir (Wien) 153, 2041–2048. https://doi.org/10.1007/s00701-
437   011-1047-9

438   Lechtreck, K.F., Delmotte, P., Robinson, M.L., Sanderson, M.J., Witman,
439   G.B., 2008. Mutations in Hydin impair ciliary motility in mice. Journal of
440   Cell Biology 180, 633–643. https://doi.org/10.1083/jcb.200710162

441   Linninger, A.A., Tangen, K., Hsu, C.Y., Frim, D., 2016. Cerebrospinal Fluid
442   Mechanics and Its Coupling to Cerebrovascular Dynamics. Annu Rev
443   Fluid Mech 48, 219–257. https://doi.org/10.1146/annurev-fluid-
444   122414-034321

445   Lun, M.P., Johnson, M.B., Broadbelt, K.G., Watanabe, M., Kang, Y.J., Chau,
446   K.F., Springel, M.W., Malesz, A., Sousa, A.M.M., Pletikos, M., Adelita,
447   T., Calicchio, M.L., Zhang, Y., Holtzman, M.J., Lidov, H.G.W., Sestan, N.,
448   Steen, H., Monuki, E.S., Lehtinen, M.K., 2015. Spatially heterogeneous

449   choroid plexus transcriptomes encode positional identity and
450   contribute to regional CSF production. Journal of Neuroscience 35,
451   4903–4916. https://doi.org/10.1523/JNEUROSCI.3081-14.2015

452   Marmarou, A., Bergsneider, M., Relkin, N., Klinge, P., Black, P.M.L., 2005.
453   INPH guidelines, part I: Development of guidelines for idiopathic
454   normal-pressure hydrocephalus: Introduction. Neurosurgery 57.
455   https://doi.org/https://doi.org/10.1227/01.NEU.0000168188.25559.0E

456   Mathew, G., Mezić, I., Petzold, L., 2005. A multiscale measure for mixing.
457   Physica D 211, 23–46. https://doi.org/10.1016/j.physd.2005.07.017

458   May, C., Kaye, J.A., Atack, J.R., Schapiro, M.B., Friedland, R.P., Rapoport, S.I.,
459   1990. Cerebrospinal fluid production is reduced in healthy aging.
460   Neurology 40, 500–500. https://doi.org/10.1017/jfm.2020.463

461   Mori, E., Ishikawa, M., Kato, T., Kazui, H., Miyake, H., Miyajima, M.,
462   Nakajima, M., Hashimoto, M., Kuriyama, N., Tokuda, T., Ishii, K.,
463   Kaijima, M., Hirata, Y., Saito, M., Arai, H., 2012. Guidelines for
464   management of idiopathic normal pressure hydrocephalus: Second
465   edition. Neurol Med Chir (Tokyo) 52, 775–778.
466   https://doi.org/10.2176/nmc.52.775

467   Nakajima, M., Yamada, S., Miyajima, M., Ishii, K., Kuriyama, N., Kazui, H.,
468   Kanemoto, H., Suehiro, T., Yoshiyama, K., Kameda, M., Kajimoto, Y.,
469   Mase, M., Murai, H., Kita, D., Kimura, T., Samejima, N., Tokuda, T.,
470   Kaijima, M., Akiba, C., Kawamura, K., Atsuchi, M., Hirata, Y., Matsumae,
471   M., Sasaki, M., Yamashita, F., Aoki, S., Irie, R., Miyake, H., Kato, T.,
472   Mori, E., Ishikawa, M., Date, I., Arai, H., 2021. Guidelines for
473   management of idiopathic normal pressure hydrocephalus (Third
474   edition): Endorsed by the Japanese society of normal pressure
475   hydrocephalus. Neurol Med Chir (Tokyo) 61, 63–97.
476   https://doi.org/10.2176/nmc.st.2020-0292

477   Nicholson, C., 1999. Signals that go with the flow. Trends Neurosci 22, 143–
478   145. https://doi.org/10.1016/S0166-2236(98)01388-5

479   Olstad, E.W., Ringers, C., Hansen, J.N., Wens, A., Brandt, C., Wachten, D.,
480   Yaksi, E., Jurisch-Yaksi, N., 2019. Ciliary Beating Compartmentalizes
481   Cerebrospinal Fluid Flow in the Brain and Regulates Ventricular
482   Development. Current Biology 29, 229-241.e6.
483   https://doi.org/10.1016/j.cub.2018.11.059

484   Otani, T., Yamashita, H., Iwata, K., Ilik, S.Y., Yamada, S., Watanabe, Y., Wada,
485   S., 2022. A concept on velocity estimation from magnetic resonance

486   velocity images based on variational optimal boundary control. Journal
487   of Biomechanical Science and Engineering 22–00050.
488   https://doi.org/10.1299/jbse.22-00050

489   Puy, V., Zmudka-Attier, J., Capel, C., Bouzerar, R., Serot, J.M., Bourgeois,
490   A.M., Ausseil, J., Balédent, O., 2016. Interactions between flow
491   oscillations and biochemical parameters in the cerebrospinal fluid.
492   Front. Aging Neurosci. 8, 1–8.
493   https://doi.org/10.3389/fnagi.2016.00154

494   Ringers, C., Olstad, E.W., Jurisch-Yaksi, N., 2020. The role of motile cilia in
495   the development and physiology of the nervous system. Philosophical
496   Transactions of the Royal Society B: Biological Sciences 375.
497   https://doi.org/10.1098/rstb.2019.0156

498   Ringstad, G., Vatnehol, S.A.S., Eide, P.K., 2017. Glymphatic MRI in idiopathic
499   normal pressure hydrocephalus. Brain 140, 2691–2705.
500   https://doi.org/10.1093/brain/awx191

501   Scollato, A., Tenenbaum, R., Bahl, G., Celerini, M., Salani, B., Di Lorenzo, N.,
502   2008. Changes in aqueductal CSF stroke volume and progression of
503   symptoms in patients with unshunted idiopathic normal pressure
504   hydrocephalus. American Journal of Neuroradiology 29, 192–197.
505   https://doi.org/10.3174/ajnr.A0785

506   Seo, J.S., Mantas, I., Svenningsson, P., Greengard, P., 2021. Ependymal cells-
507   CSF flow regulates stress-induced depression. Mol Psychiatry 26, 7308–
508   7315. https://doi.org/10.1038/s41380-021-01202-1

509   Shanks, J., Markenroth Bloch, K., Laurell, K., Cesarini, K.G., Fahlström, M.,
510   Larsson, E.M., Virhammar, J., 2019. Aqueductal CSF stroke volume is
511   increased in patients with idiopathic normal pressure hydrocephalus
512   and decreases after shunt surgery. American Journal of Neuroradiology
513   40, 453–459. https://doi.org/10.3174/ajnr.A5972

514   Shook, B.A., Lennington, J.B., Acabchuk, R.L., Halling, M., Sun, Y., Peters, J.,
515   Wu, Q., Mahajan, A., Fellows, D.W., Conover, J.C., 2014.
516   Ventriculomegaly associated with ependymal gliosis and declines in
517   barrier integrity in the aging human and mouse brain. Aging Cell 13,
518   340–350. https://doi.org/10.1111/acel.12184

519   Sincomb, S., Coenen, W., Sánchez, A.L., Lasheras, J.C., 2020. A model for the
520   oscillatory flow in the cerebral aqueduct. J Fluid Mech.
521   https://doi.org/10.1017/jfm.2020.463

522 Siyahhan, B., Knobloch, V., De Zélicourt, D., Asgari, M., Daners, M.S.,
523   Poulikakos, D., Kurtcuoglu, V., 2014. Flow induced by ependymal cilia
524   dominates near-wall cerebrospinal fluid dynamics in the lateral
525   ventricles. J R Soc Interface 11. https://doi.org/10.1098/rsif.2013.1189

526 Skipor, J., Thiery, J.C., 2008. The choroid plexus - cerebrospinal fluid system:
527   Undervalued pathway of neuroendocrine signaling into the brain.
528   Acta Neurobiol Exp (Wars) 68, 414–428.

529 Sotelo, J., Urbina, J., Valverde, I., Tejos, C., Irarrázaval, P., Hurtado, D.E.,
530   Uribe, S., 2015. Quantification of wall shear stress using a finite-
531   element method in multidimensional phase-contrast MR data of the
532   thoracic aorta. J Biomech 48, 1817–1827.
533   https://doi.org/10.1016/j.jbiomech.2015.04.038

534 Sweetman, B., Xenos, M., Zitella, L., Linninger, A.A., 2011. Three-
535   dimensional computational prediction of cerebrospinal fluid flow in the
536   human brain. Comput Biol Med 41, 67–75.
537   https://doi.org/10.1016/j.compbiomed.2010.12.001

538 Wentland, A.L., Wieben, O., Korosec, F.R., Haughton, V.M., 2010. Accuracy
539   and reproducibility of phase-contrast MR imaging measurements for
540   CSF flow. American Journal of Neuroradiology 31, 1331–1336.
541   https://doi.org/10.3174/ajnr.A2039

542 Yamada, S., Ishikawa, M., Ito, H., Yamamoto, K., Yamaguchi, M., Oshima, M.,
543   Nozaki, K., 2020. Cerebrospinal fluid dynamics in idiopathic normal
544   pressure hydrocephalus on four-dimensional flow imaging. Eur Radiol
545   30, 4454–4465. https://doi.org/10.1007/s00330-020-06825-6

546 Yamada, S., Ito, H., Ishikawa, M., Yamamoto, K., Yamaguchi, M., Oshima, M.,
547   Nozaki, K., 2021. Quantification of Oscillatory Shear Stress from
548   Reciprocating CSF Motion on 4D Flow Imaging. American Journal of
549   Neuroradiology 1–8. https://doi.org/10.3174/ajnr.a6941

550 Yamada, S., Miyazaki, M., Yamashita, Y., Ouyang, C., Yui, M., Nakahashi, M.,
551   Shimizu, S., Aoki, I., Morohoshi, Y., Mccomb, J.G., 2013. Influence of
552   respiration on cerebrospinal fluid movement using magnetic resonance
553   spin labeling. Fluids Barriers CNS 10, 1–7.
554   https://doi.org/10.1186/2045-8118-10-36

555 Yavuz Ilik, S., Otani, T., Yamada, S., Watanabe, Y., Wada, S., 2022. A subject-
556   specific assessment of measurement errors and their correction in
557   cerebrospinal fluid velocity maps using 4D flow MRI. Magn Reson Med
558   87, 2412–2423. https://doi.org/10.1002/mrm.29111

559 Zappaterra, M.D., Lisgo, S.N., Lindsay, S., Gygi, S.P., Walsh, C.A., Ballif, B.A.,
560   2007. A comparative proteomic analysis of human and rat embryonic
561   cerebrospinal fluid. J Proteome Res 6, 3537–3548.
562   https://doi.org/10.1021/pr070247w

563 Zhangyang, W., Yiying Zhang, Fan Hu, Jing Ding, Xin Wang, 2020.
564   Pathogenesis and pathophysiology of idiopathic normal pressure
565   hydrocephalus. CNS Neurosci Ther 1230–1240.
566   https://doi.org/10.1111/cns.13526

567 Zhou, X., Xia, J., 2022. Application of Evans Index in Normal Pressure
568   Hydrocephalus Patients: A Mini Review. Front Aging Neurosci.
569   https://doi.org/10.3389/fnagi.2021.783092

570

571

572   Table 1 Basal geometric properties of all subjects (Left ventricle: LV, Third ventricle: 3V, Fourth

573   ventricle: 4V). Evans index is used to evaluate ventriculomegaly, and hydrocephalus is defined

574   as > 0.3 (Nakajima et al., 2021).

Case	LV volume [ml]	3V volume [ml]	4V volume [ml]	Evans index
control1	37.4	1.6	2.6	0.276
control2	27.4	1.4	1.6	0.254
control3	18.3	1.1	1.6	0.240
control4	18.9	1.3	2.2	0.249
control5	19.6	1.0	1.7	0.259
control6	10.8	1.3	1.9	0.221
control7	17.2	1.5	1.9	0.255
control8	24.3	0.7	1.4	0.270
control9	7.2	0.8	0.9	0.236
control10	16.7	0.9	1.4	0.225
iNPH1	138.8	4.3	2.5	0.373
iNPH2	104.4	3.9	2.6	0.329
iNPH3	99.7	4.5	3.5	0.329
iNPH4	104.6	6.4	2.5	0.301
iNPH5	61.7	2.4	1.6	0.301
iNPH6	71.9	4.0	1.9	0.318
iNPH7	152.5	6.0	4.7	0.384
iNPH8	165.9	5.0	4.2	0.342
iNPH9	114.2	4.1	4.4	0.332
iNPH10	83.5	4.8	2.2	0.373
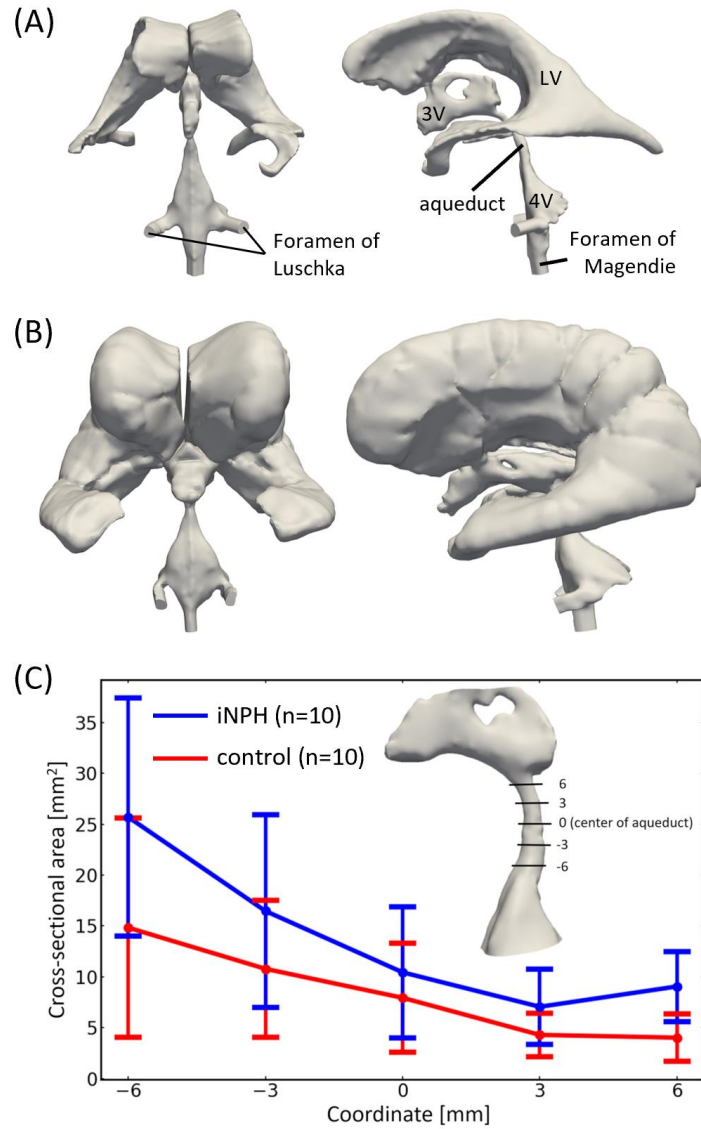
Fig. 1. Geometries of the cerebral ventricles of a healthy control (A) and an idiopathic normal pressure hydrocephalus (iNPH) patient (B), reconstructed from T2-weighted magnetic resonance images, and the cross-sectional area of the cerebral aqueduct (mean ± S.D.) along its length (C) in healthy controls (red line) and iNPH patients (blue line).

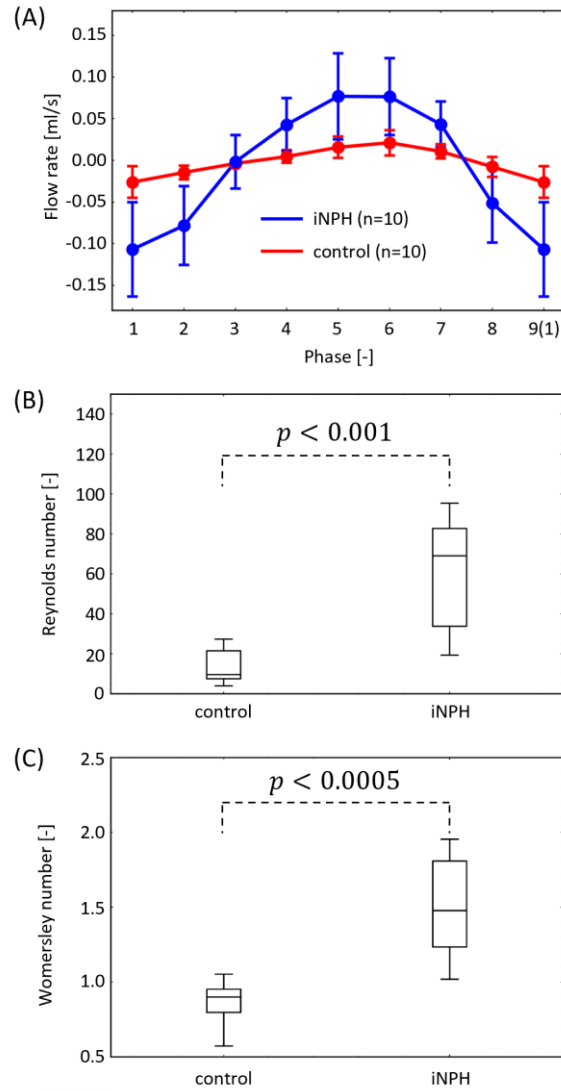LV: lateral ventricle, 3V: third ventricle, 4V: fourth ventricle.

582

583   Fig. 2. Time course of the cerebrospinal fluid (CSF) flow rate through the aqueduct (A) in healthy

584   controls and iNPH patients (mean ± S.D.). Maximum Reynolds number on the cross-sectional

585   plane in the aqueduct (B) and associated Womersley number (C). A Mann–Whitney U test was

586   used to compute p values.

587

588
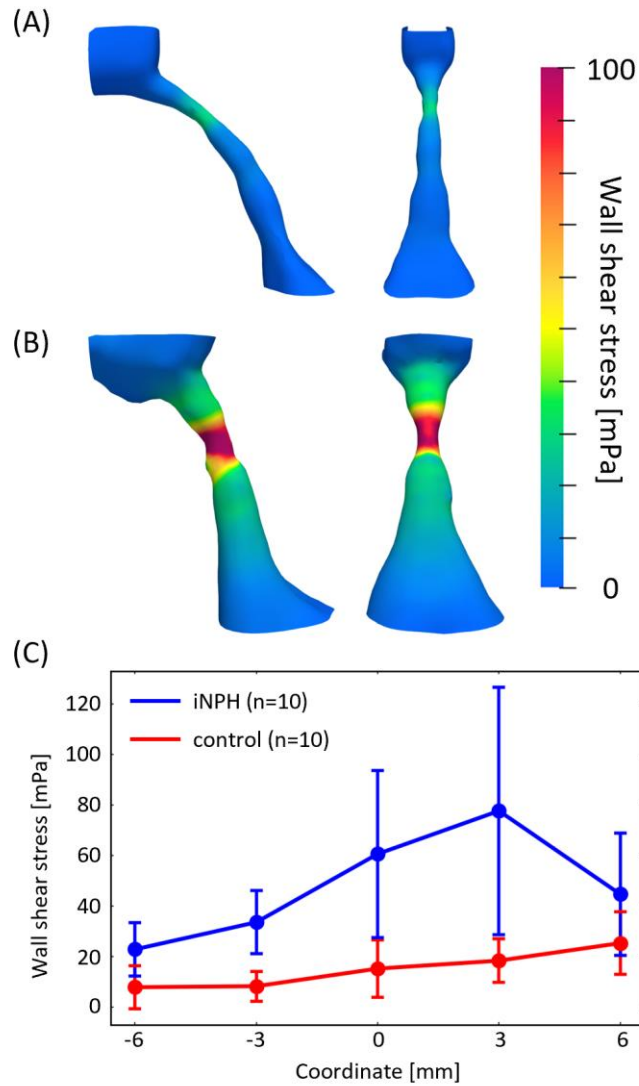
Fig. 3. Wall shear stress distributions on the cerebral aqueduct wall in a representative healthy control (A) and iNPH patient (B), and wall shear stress distributions in the aqueduct (mean ± S.D.) along its length (C) in healthy controls (red line) and iNPH patients (blue line). The definition of the coordinate is the same as that in Fig. 1 (C).
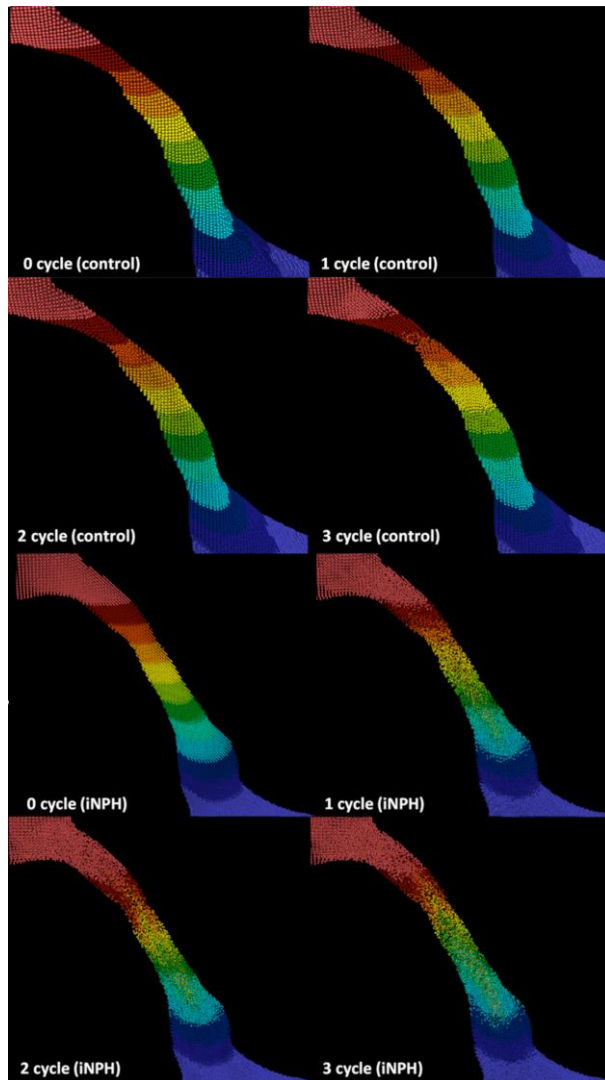
593

Fig. 4. Time course of the three-dimensional particle tracer distributions in the cerebral aqueduct in a representative healthy control (top) and iNPH patient (bottom) in the left-side view. The color of the particle tracer is set according to its initial position. Videos of the time course are shown in Electronic supplementary material 7 (control) and 8 (iNPH).
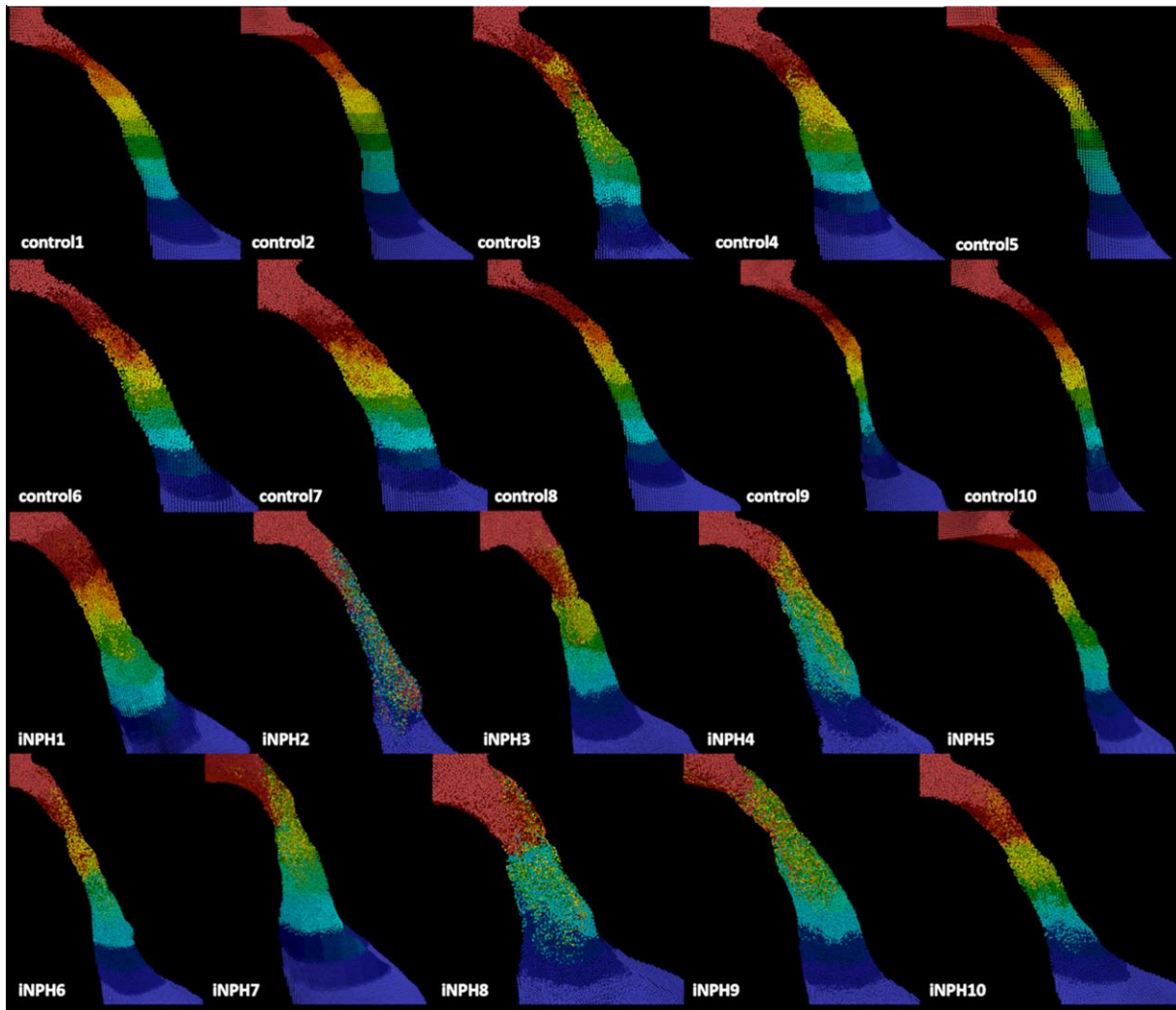
594

595

596

597

598

Fig. 5. Three-dimensional particle tracer distributions in the cerebral aqueduct after 20 cardiac cycles in healthy controls (top) and iNPH patients (bottom) in the left-side view.
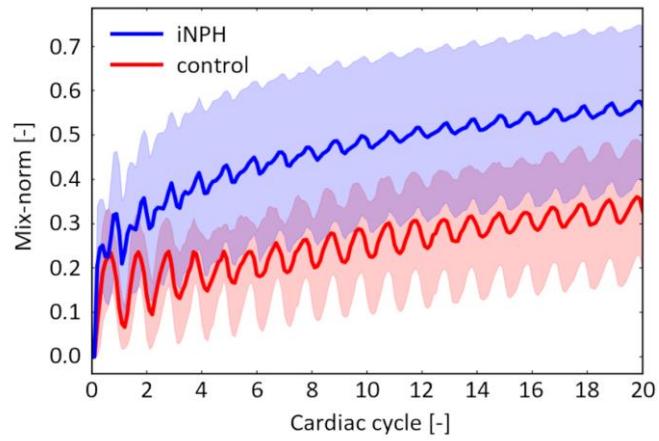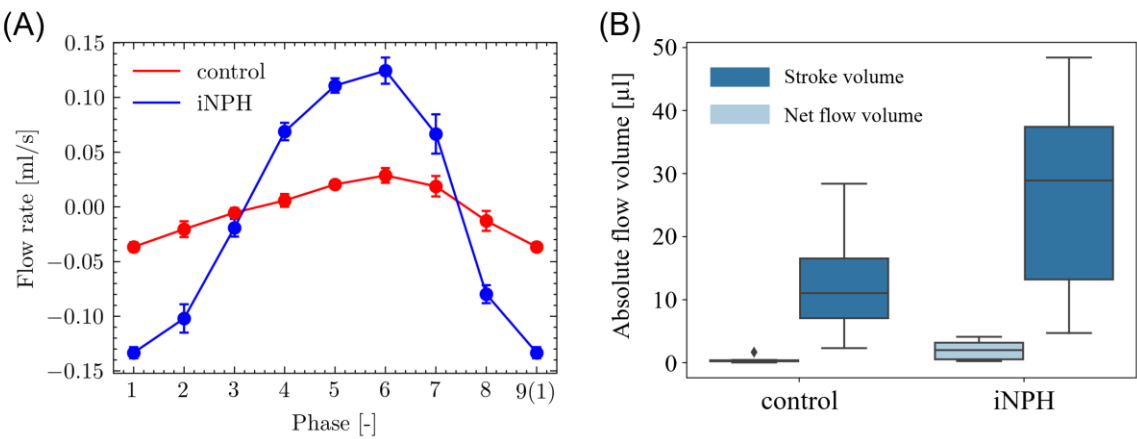
603

604   Fig. 6. Time course of the average mix-norm in the cerebral aqueduct in healthy controls (red)

605   and iNPH patients (blue). The shaded area represents the standard deviation.

606

607

608

609 Fig. A1 (A) Time courses of the cerebrospinal fluid (CSF) flow rate (mean ± S.D.) among four cross-

610 sectional planes in the aqueduct in a representative control (red) and an iNPH patient (blue) and

611 (B) box plots of net CSF flow volume and stroke volume for a cardiac cycle in all healthy controls

612 (left) and iNPH patients (left).

613